

1 **Ocean bottom distributed acoustic sensing for *T*-wave detection and seismic ocean**  
2 **thermometry**

3 **Zhichao Shen<sup>1</sup> and Wenbo Wu<sup>1</sup>**

4 <sup>1</sup>Department of Geology and Geophysics, Woods Hole Oceanographic Institution, Woods Hole,  
5 MA, USA

6 Corresponding author: Zhichao Shen ([zhichao.shen@whoi.edu](mailto:zhichao.shen@whoi.edu))

7 **Key Points:**

- 8     • We develop a curvelet denoising scheme for ocean bottom distributed acoustic sensing to  
9     enhance *T*-wave signals.
- 10    • Distributed acoustic sensing using the OOI cable records 92 *T*-wave events, tripling the  
11    detections of the Canada Neptune Ocean Network.
- 12    • The improved detection capability makes more small repeating earthquakes usable for  
13    seismic ocean thermometry.

**14 Abstract**

15 A *T*-wave is a seismo-acoustic wave that can travel a long distance in the ocean with little  
16 attenuation, making it valuable for monitoring remote tectonic activity and changes in ocean  
17 temperature using seismic ocean thermometry (SOT). However, current high-quality *T*-wave  
18 stations are sparsely distributed, limiting the detectability of marine seismicity and the spatial  
19 resolution of global SOT. The use of ocean bottom distributed acoustic sensing (OBDAS), through  
20 the conversion of telecommunication cables into dense seismic arrays, is a cost-effective and  
21 scalable means to complement existing seismic stations. Here, we systematically investigate the  
22 performance of OBDAS for *T*-wave detection and SOT using a 4-day Ocean Observatories  
23 Initiative community experiment offshore Oregon. We first present *T*-wave observations from  
24 distant and regional earthquakes, and then develop a curvelet denoising scheme to enhance *T*-wave  
25 signals on OBDAS. Curvelet denoising enables us to detect 92 oceanic earthquakes during the 4-  
26 day experiment, most of which are missing from existing global catalogs and from the regional *T*-  
27 wave catalog compiled using Ocean Networks Canada stations. With a single cable, OBDAS  
28 allows us to effectively constrain the azimuth of detected seismicity via array beamforming. We  
29 further evaluate the SOT performance of OBDAS using pseudo-repeating earthquake *T*-waves.  
30 Our results show that OBDAS can utilize repeating earthquakes as small as M3.5 for SOT,  
31 outperforming ocean bottom seismometers. However, ocean ambient natural and instrumental  
32 noise strongly affects the performance of OBDAS for *T*-wave detection and SOT, requiring further  
33 investigation.

**34 Plain Language Summary**

35 Submarine earthquakes can produce loud sounds in the ocean. These sounds usually arrive at a  
36 seismic station as the tertiary wave, a so-called *T*-wave, following the arrival of the primary *P*-  
37 wave and secondary *S*-wave. *T*-waves can propagate thousands of kilometers in the ocean's  
38 SOFAR (SOund Fixing And Ranging) channel with little energy loss. Thus, they are useful for  
39 monitoring earthquakes and ocean temperature changes. However, currently available instruments  
40 for measuring these waves are limited. Recently, a new type of technique, Distributed Acoustic  
41 Sensing (DAS), provides an opportunity to expand the seismic-recording capability in the ocean.  
42 Ocean bottom distributed acoustic sensing (OBDAS) can effectively turn submarine  
43 telecommunication cables into dense seismic sensors that complement conventional seismometers.  
44 In this study, we explore the OBDAS potential for *T*-wave detection. With a 4-day OBDAS  
45 community experiment offshore Oregon, we demonstrate that OBDAS does a better job than a  
46 conventional seismic network for detecting *T*-waves when a specifically designed denoising  
47 scheme is applied. In addition, OBDAS has the potential to measure ocean temperature changes  
48 using more repeating earthquakes of smaller magnitudes, outperforming conventional sensors.  
49 However, the accuracy of the OBDAS system can be strongly affected by various types of noise,  
50 which requires further research.

## 51 **1 Introduction**

52 As a tertiary arrival after the *P*-wave and *S*-wave on seismograms, the seismo-acoustic *T*-wave  
53 propagates horizontally at a speed of  $\sim 1.5$  km/s along the ocean SOund Fixing And Ranging  
54 (SOFAR) channel, where ocean sound speed reaches a minimum (Tolstoy & Ewing, 1950;  
55 Linehan, 1940). Generated from earthquakes and a number of acoustic sources in the water column,  
56 *T*-waves can travel a long distance ( $>1000$  km) with little energy loss. *T*-waves exhibit spindle-  
57 shaped, high-frequency ( $>1$  Hz) waveforms on hydrophones (Fox et al, 1995), ocean bottom  
58 seismometers (OBS; Hamada, 1985), autonomous MERMAID floats (Simon et al., 2021), and  
59 even land stations (e.g., Buehler & Shearer, 2015). Since their early documentations in the 1930s  
60 (Jagger, 1930; Collins, 1936), *T*-waves have been widely used to monitor submarine seismicity  
61 (Fox et al., 2001; Smith et al., 2002; Dziak et al, 2004; Hanson & Bowman, 2006; Parnell-Turner  
62 et al., 2022) and volcanism (Wech et al, 2018; Tepp & Dziak, 2021), promote tsunami warning  
63 (Okal & Talandier, 1986; Matsumoto et al., 2016), determine earthquake properties (Walker et al.,  
64 1992; de Groot-Hedlin, 2005), discriminate explosive and seismic sources (Talandier & Okal,  
65 2001, 2016), infer detached slabs (Okal, 2001), and constrain crustal attenuation (Koyanagi et al.,  
66 1995; Zhou et al., 2021), significantly broadening our understanding of tectonic process in the  
67 remote ocean (Dziak et al., 2012) and seismo-acoustic wave genesis and propagation (Okal, 2008).

68 *T*-waves can also provide valuable insights to long-term deep ocean temperature changes. With  
69 more than 90% of excess heat due to the greenhouse effect being absorbed, the ocean is  
70 experiencing a secular warming trend of  $\sim 0.02$  K per decade (Wunsch, 2016). Since the ocean is  
71 an efficient hydroacoustic transmitter and sound speed in seawater increases with temperature, Wu  
72 et al. (2021) developed seismic ocean thermometry (SOT) to quantify basin-scale ocean  
73 temperature changes from the travel time changes of *T*-waves generated by repeating earthquakes.  
74 This idea was inspired by the ocean acoustic tomography proposed by Munk and Wunsch (1979).  
75 While the latter concept, which utilizes active sources, has achieved great success (Munk et al.,  
76 1994; ATOC Consortium, 1998), the cost-efficient SOT approach has shown great potential to  
77 complement modern Argo Climatology data (Riser et al., 2016) in a passive way. Applying SOT  
78 to the equatorial Indian Ocean revealed ocean dynamic signals at various time scales and depths  
79 including seasonal changes, meso-scale eddies and equatorial waves (Wu et al., 2021; Callies et  
80 al., 2023), that demonstrates its potential to complement existing ocean temperature observations.

81 A further expansion of SOT to the global ocean requires the establishment of long-term stations to  
82 record high-quality *T*-waves from repeating earthquakes. However, suitable *T*-wave stations  
83 remain sparsely distributed, the Comprehensive Nuclear-Test-Ban Treaty Organization (CBTBO)  
84 operating a handful of hydrophone stations (Figure 1a), and with other networks maintaining a few  
85 island stations and a limited number of offshore cabled sites, greatly limiting the spatial coverage  
86 of global SOT. In particular, the coverage of the Arctic and Southern Oceans (Figure 1a) is  
87 extremely poor, highlighting an urgent need for more observations to fill the gap. Meanwhile,

88 deploying and maintaining long-term, high-quality *T*-wave instrumentation in the harsh ocean  
89 environment is a significant logistical and financial challenge.

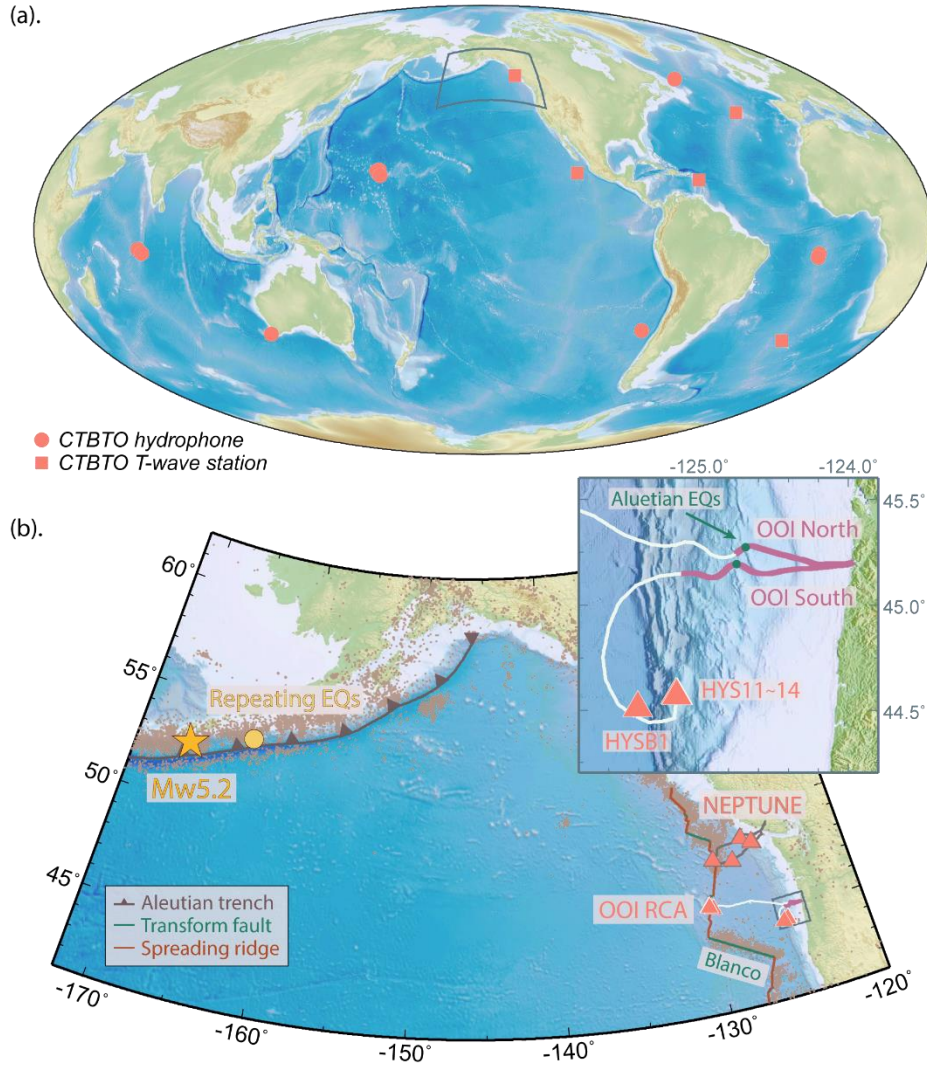
90 Distributed acoustic sensing (DAS) is a new and promising technology that offers a cost-efficient  
91 and scalable solution for deploying large-aperture, long-term, dense seismic arrays. By converting  
92 Rayleigh-type backscattering due to intrinsic fiber impurities to longitudinal strain or strain rate,  
93 DAS repurposes pre-existing telecommunication fiber-optic cables into arrays of thousands of  
94 vibration sensors (Hartog, 2017). With up to ~100 km aperture and sensor spacing of a few meters,  
95 DAS can record high frequency wavefields at unprecedented spatiotemporal resolution, making it  
96 a compelling tool for a range of geophysical settings (Zhan, 2020; Lindsey & Martin, 2021). In  
97 underwater environments, ocean bottom DAS (OBDAS) has been successfully used as a very  
98 broadband instrument (Ide et al., 2021) to detect earthquakes (Lior et al., 2021), illuminate seafloor  
99 faults (Lindsey et al., 2019), characterize marine sediment (Spica et al., 2020; Cheng et al., 2021;  
100 Viens et al., 2022), monitor ocean dynamics (Sladen et al., 2019; Williams et al., 2019, 2022) and  
101 map offshore wind turbines (Williams et al., 2021). With air-gun shots, Matsumoto et al., (2021)  
102 demonstrated that OBDAS is effective in sensing hydroacoustic signals across a broad frequency  
103 range from a tenth to a few tens of Hz. Recently, Ugalde et al., (2022) presented *T*-wave  
104 observations on OBDAS in the Canary Islands from several regional and distant earthquakes.  
105 However, due to limited observations, the performance of OBDAS for *T*-wave detection and SOT  
106 has not yet been systematically investigated.

107 In this study, we use data from a 4-day community experiment conducted offshore central Oregon  
108 to examine *T*-waves on OBDAS. To identify potential *T*-wave candidates on OBDAS, we first  
109 build a *T*-wave catalog using Ocean Networks Canada cabled OBS and hydrophone array. With  
110 this catalog, we identify *T*-wave observations on OBDAS and develop a curvelet denoising  
111 algorithm to enhance *T*-wave signal-to-noise ratios. The application of curvelet denoising on  
112 OBDAS enables us to detect 92 *T*-wave events, three times the number identified in the NEPTUNE  
113 *T*-wave catalog. With the enhanced detection capability, we propose a new workflow for SOT with  
114 OBDAS, taking advantage of a larger number of usable small repeating earthquakes compared to  
115 the OBS data. Looking forward, we also discuss earthquake location resolvability using OBDAS  
116 and the noise in OBDAS data.

## 117 **2 Data**

118 The Ocean Observatory Initiative (OOI) Regional Cable Array (RCA) offshore central Oregon is  
119 a long-term infrastructure designed to facilitate integrated investigations into both volcanic and  
120 coastal systems (Kelly et al., 2014). It provides real-time telemetry for over 140 instruments,  
121 including OBSs, remote access fluid samplers, DNA samplers, acoustic doppler current profilers  
122 and so on. The OOI RCA observatory is powered by and communicates through two  
123 telecommunication fiber-optic subsea backbone cables, with the northern branch extending to  
124 Axial Seamount and the southern branch running to the Oregon shelf (Figure 1b). Since 2015, five

125 OBSs have been deployed near Southern hydrate ridge (Figure 1b) in order to monitor marine  
 126 seismicity, track melt migration, and whale vocalizations, with four located at the ridge summit at  
 127 a water depth of ~800 m (HYS11-14) and one situated at the slope base at a water depth of ~2900  
 128 m (HYSB1).



129  
 130 **Figure 1.** The CTBTO hydrophone network and our study region. (a). Global CTBTO  
 131 hydrophones and *T*-wave stations. The gray box illustrates our study region. (b). Map view of our  
 132 study region with background tectonics and seismicity, cabled ocean observatories (ONC  
 133 NEPTUNE and OOI RCA; orange triangles), and OOI OBDA. The insert panel (top right) is a  
 134 zoom-in view of OBDA (purple lines) and OBSs at OOI. The green dots indicate the locations  
 135 where the OOI North and South cables turn southward. White lines denote entire backbone cables.  
 136 The green arrow represents the *T*-wave propagation direction from Aleutian earthquakes.

137 During a scheduled maintenance period of the OOI RCA platform in November 2021, a four-day  
 138 community experiment was conducted to explore the potential of submarine DAS for observing  
 139 seismic, oceanographic, acoustic, and geodetic processes (Wilcock et al., 2023). Specifically,

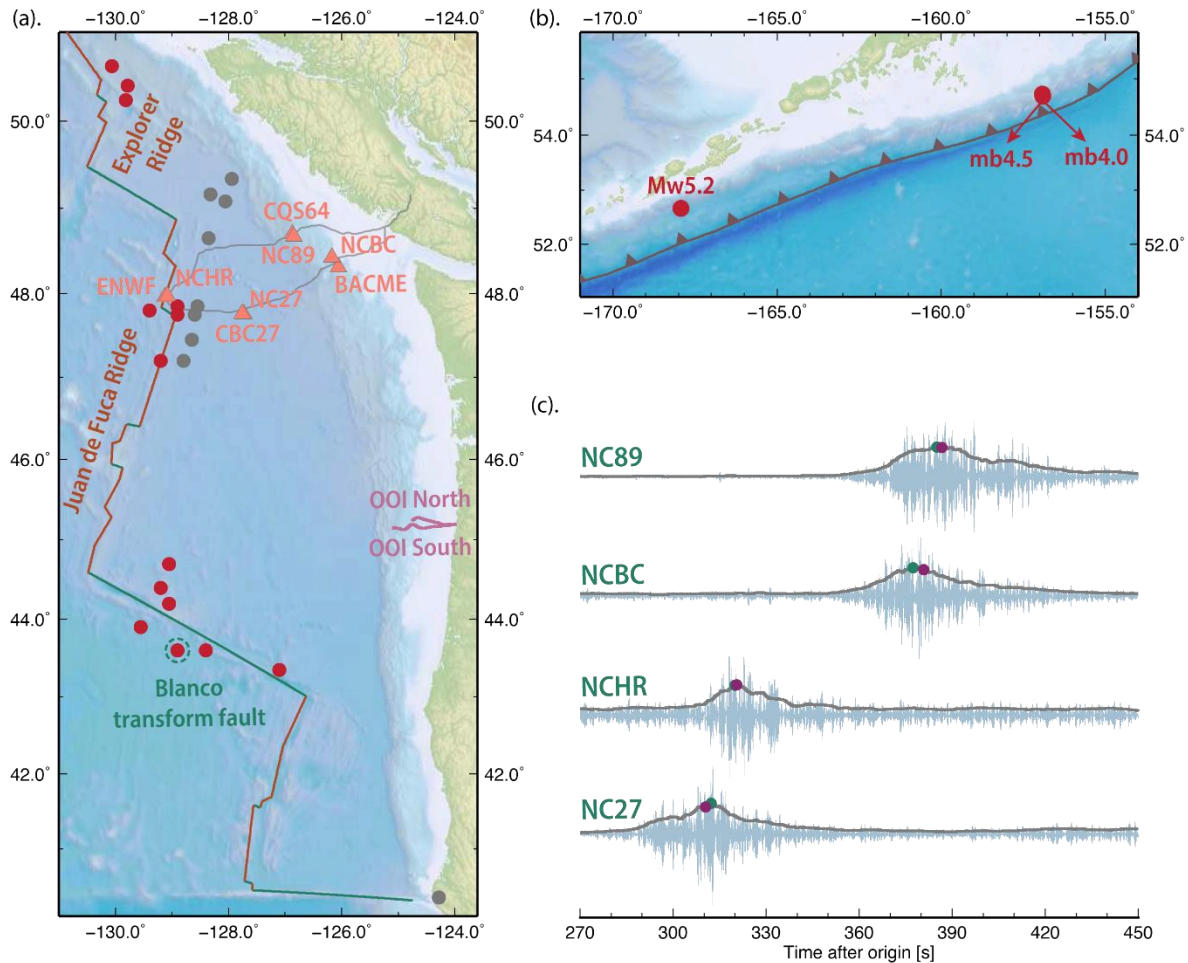
140 between November 1<sup>st</sup> and 5<sup>th</sup>, two fiber-optic backbone cables were temporarily converted to  
141 OBDAS arrays, referred to as OOI North and OOI South. The OOI North array had two optical  
142 fibers connected to Optasense QuantX and Silixa iDASv3 interrogators, respectively, to record  
143 OBDAS data up to the first optical repeater located at ~65 km from the shore, with a gauge length  
144 of 30 m during most of the experiment. OOI South had one fiber for collecting OBDAS data using  
145 another Optasense QuantX interrogator, while the other fiber was used for distributed temperature  
146 sensing. The first optical repeater of OOI South is located ~95 km away, and the gauge length is  
147 set at 50 m. With a channel spacing of ~2 m, the OOI North array has a total number of 32,600  
148 channels whereas the OOI South array consists of 47,500 channels. During the experiment, both  
149 arrays recorded abundant low-frequency acoustic signals such as whale calls and ship noise  
150 (Wilcock et al, 2023). In this study, we solely focus on the Optasense OBDAS data since the data  
151 from both arrays are available, allowing for a direct and straightforward comparison.

152 Located ~400 km northeast of the RCA network, the Ocean Networks Canada (ONC) North-East  
153 Pacific Undersea Networked Experiments (NEPTUNE) off the coast of British Columbia is  
154 another multidisciplinary observatory that has been used to monitor the earth/ocean system since  
155 2009. The NEPTUNE network consists of more than 14 ocean bottom seismometers,  
156 accelerometers and hydrophones that are mainly distributed across four sites: Clayoquot Slope,  
157 Endeavour Ridge, Cascadia Basin, and Barkley Canyon (Barnes et al., 2008; Figure 1b). Both the  
158 OOI and NEPTUNE networks have high sensitivity to *T*-waves from earthquakes at mid-ocean  
159 ridges and transform faults in the northeast Pacific and the Aleutian subduction zone (Dziak et al.,  
160 2012; Tréhu et al., 2018).

### 161 **3 NEPTUNE *T*-wave catalog**

162 During the four-day community DAS experiment, the global ISC (International Seismological  
163 Centre; Bondár & Storchak, 2011) catalog only documents a few earthquakes in the northeast  
164 Pacific that might produce high-quality *T*-waves (Table S1). To search for a more complete set of  
165 *T*-wave events, we download vertical component seismograms from eight NEPTUNE stations,  
166 with two at each site (Figure 2a), remove their instrument responses, mean values and linear trends,  
167 and band-pass filter the data between 4 and 6 Hz, which is favorable for high-quality *T*-wave  
168 observations (Okal, 2008). We implement a recursive short-time-average/long-time-average  
169 (STA/LTA) algorithm (Withers et al., 1998) to detect *T*-waves on each individual station. With a  
170 STA of 5 s and LTA of 50 s, potential *T*-waves are identified once their STA/LTA ratios exceed a  
171 threshold of 1.8, which corresponds to ~12 times the median absolute deviation of daily STA/LTA.  
172 We then clean all the picks in a 50-s sliding window and only retain detections if *T*-waves are  
173 observed at more than three sites (Figure 2c). After careful visual examinations, we establish a  
174 total of 27 *T*-wave events (Table S1). Our NEPTUNE catalog includes six earthquakes in the ISC  
175 catalog with three M4.0+ events in the Aleutian trench, two small ones north of NEPTUNE and a

176 Mw4.4 event near the coast of Northern California (Figure 2; Table S1), confirming the robustness  
 177 of our method.



178  
 179 **Figure 2.** Ocean Networks Canada NEPTUNE  $T$ -wave catalog. (a). Regional seismicity detected  
 180 using  $T$ -waves at the NEPTUNE networks. The red and gray circles indicate earthquakes with  
 181 detectable and undetectable  $T$ -waves on OOI OBDAS, respectively. The green dashed circle  
 182 denotes the event shown in (c). (b). Similar to (a) but for earthquakes along the Aleutian trench.  
 183 (c).  $T$ -waves detected on the NEPTUNE array from a Blanco earthquake. The gray lines indicate  
 184  $T$ -wave envelopes smoothed by a 5-s sliding window. The green and purple solid circles represent  
 185 the picked and predicted  $T$ -wave arrivals (envelope peaks), respectively.

186 We find four events not in the ISC catalog that generate clear  $P$ -waves and  $S$ -waves at nearby  
 187 onshore stations (Figure S1). To determine their origin times and locations, we perform a grid  
 188 search with an interval of  $0.02^\circ$ , minimizing the L1 norm of the time differences between predicted  
 189 and manually picked  $P$  and  $S$  arrivals (see supplementary text S1 for more details; Kennett &  
 190 Engdahl, 1991). All of them are located in regions of active background seismicity close to the  
 191 continental shelf – two near the Explorer Ridge and the other two to the north of the NEPTUNE  
 192 array (Figures 2a and S1). Given the optimal locations, we estimate their local magnitudes (ML)

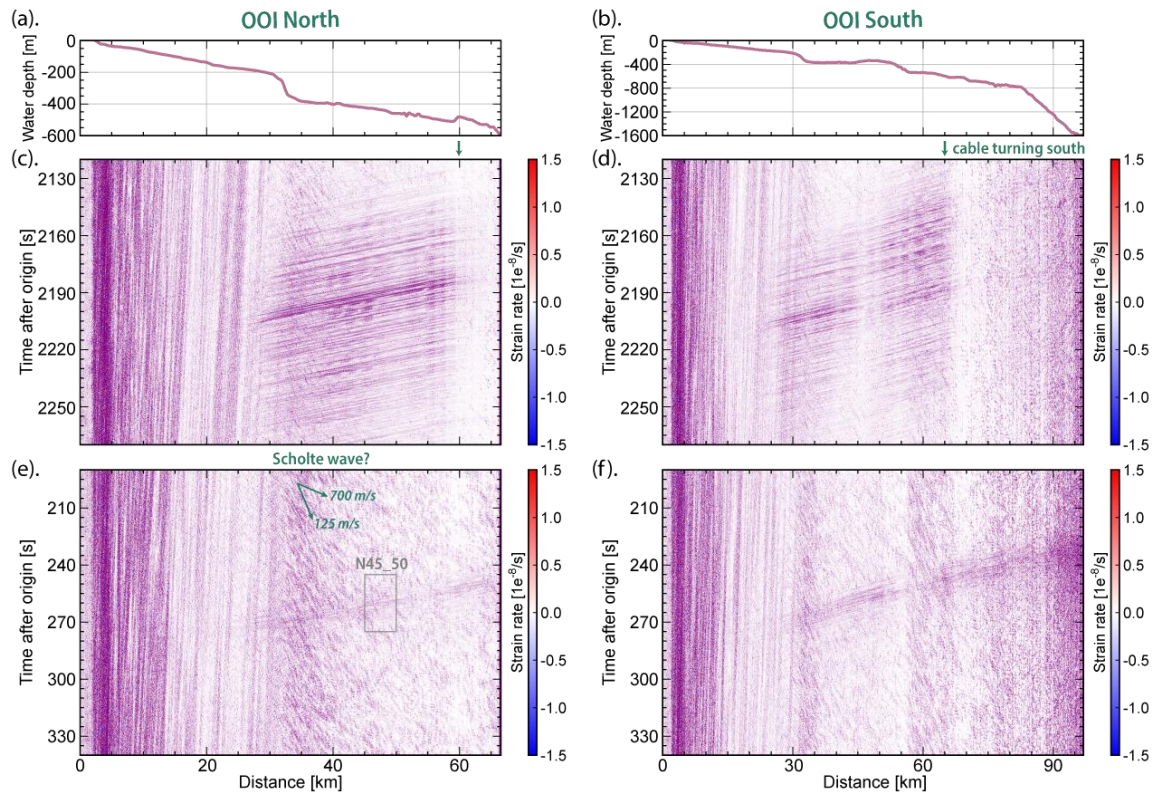
193 by averaging over all the stations in a frequency band of 2-10 Hz (Bakun & Joyner, 1984). The  
194 resulting magnitudes, ranging from ML1.6 to ML2.3, are too small to be detected in the ISC  
195 catalog (Table S1). For the remaining events without clear P and S observations at onshore stations,  
196 we use the arrival times of *T*-wave envelope peaks to determine event locations (Figures 2c and  
197 S1). Compared to *P*-waves and *S*-waves, *T*-waves are excited within a broad area near the source  
198 (Okal, 2008) and consequently less sensitive to earthquake locations, so we limit the grid search  
199 to seismically active regions and use a relatively larger interval of  $0.05^\circ$ . Given that oceanic  
200 earthquakes are typically shallow and *T*-wave arrival time has little sensitivity to depth, the focal  
201 depth is fixed at 10 km. The results suggest that most events reflect local seismicity near the  
202 NEPTUNE array, while seven of them are from the Blanco transform fault (Figure 2; Table S1).  
203 We do not determine the magnitudes of the seven Blanco events since a robust magnitude estimate  
204 using *T*-wave is challenging (Okal, 2008). However, a previous study by Fox et al. (1993)  
205 suggested that detectable *T*-wave events at similar distances are generally of magnitude M2.0+.  
206 Overall, our four-day catalog includes many more events compared to the global ISC catalog and  
207 provides us with prior knowledge to search for *T*-waves on OOI OBDAS.

## 208 **4 OBDAS for *T*-wave detections**

### 209 **4.1 *T*-wave observations at OOI OBDAS**

210 With the new catalog, we visually scrutinize the *T*-waves on OBDAS for each event at 4-6 Hz, the  
211 same frequency band used for the NEPTUNE *T*-wave observations. Most of the events, except for  
212 those near the NEPTUNE array, excite visible *T*-waves at OOI North and OOI South (Figure 2;  
213 Table S1). In particular, a Mw5.2 Fox islands earthquake, the largest event in our NEPTUNE  
214 catalog, generates clear *T*-waves with a duration of  $>150$  s on the 25-60 km portion of OOI North  
215 (N25\_60) and 20-65 km segment of OOI South (S20\_65; Figures 3c and 3d). Intriguingly, the  
216 wavefields exhibit a sharp drop of *T*-wave energy at distances of  $\sim 60$  km on OOI North and  $\sim 65$   
217 km on OOI South (Figure 3), where the cable orientations become more perpendicular to the *T*-  
218 wave propagation direction (Figure 1b). The decreases in *T*-wave energy could be attributed to the  
219 directional sensitivity of OBDAS – the radial strain converted from the acoustic pressure of a *T*-  
220 wave would be reduced when the incoming wave propagation direction becomes perpendicular to  
221 the cable orientation (Martin et al., 2021; Fang et al., 2023). Another possible explanation for the  
222 weaker *T*-wave observation could be elevated bathymetry blocking the wave propagation to the  
223 seafloor. However, the latter interpretation may not be applicable here as no obvious elevated  
224 bathymetry is present. In contrast, earthquakes from the Blanco transform fault exhibit more  
225 continuous *T*-wave wavefields across both cables (Figures 3e and 3f), favoring our former  
226 interpretation of directional sensitivity. Compared to the Mw5.2 Fox islands earthquake, the  
227 Blanco event produces *T*-waves with shorter durations and lower signal-to-noise ratios (SNR) due  
228 to its smaller magnitude (Figure 3). In both cases, *T*-waves consistently exhibit lower SNRs at  
229 cable distances less than 30 km (Figure 3), which can be attributed to two main factors. Firstly, the

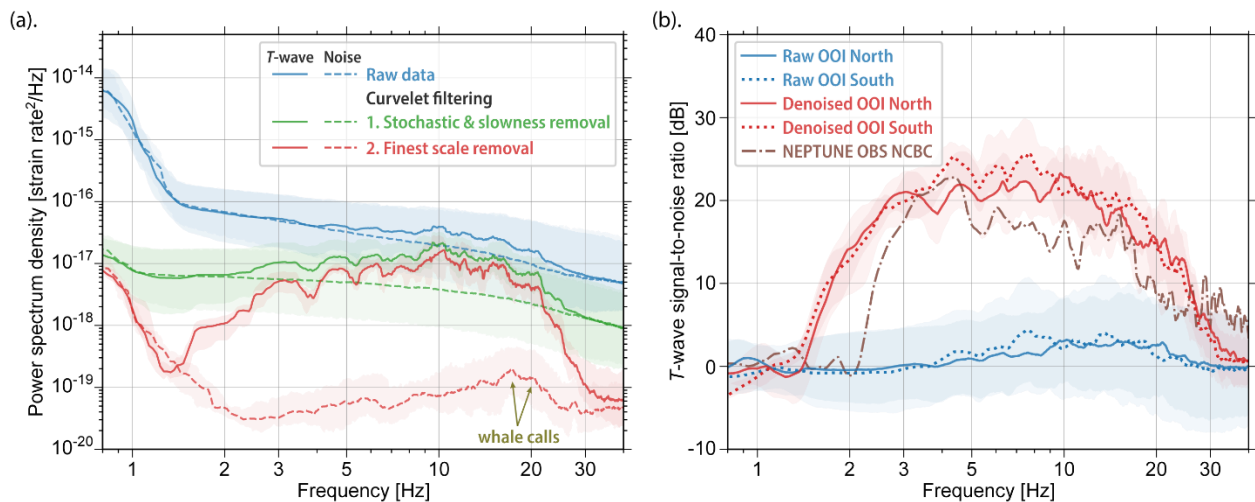
230 presence of strong background noise associated with ocean gravity waves significantly  
 231 contaminates the *T*-wave signal. Secondly, as the *T*-wave propagates towards the coast, it  
 232 undergoes complex interactions with the seafloor, leading to dramatic signal attenuation.



233  
 234 **Figure 3.** 4-6 Hz *T*-waves on the OOI OBDAS arrays. (a). Water depth along OOI North. (b).  
 235 Water depth along OOI South. (c). The 4-6 Hz *T*-wave on OOI North from the Mw5.2 Fox islands  
 236 earthquake. (d). Similar to (c) but for OOI South. (e). The 4-6 Hz *T*-wave on OOI North from a  
 237 Blanco earthquake that occurred on November 4<sup>th</sup>, 2021 (dashed circle in Figure 2a; Event No. 25  
 238 in Table S1). The grey box N40\_45 denotes the wavefield used in Figures 4 and 6. (f). Similar to  
 239 (e) but for OOI South.

240 As a relatively new instrument for underwater environment, OBDAS can in fact record *T*-waves  
 241 across a broad frequency band, extending beyond the 4-6 Hz range, but with lower SNRs. Taking  
 242 the Blanco earthquake as an example, we calculate the noise and *T*-wave spectra of individual  
 243 OBDAS channels on the 45-50 km segment of OOI North (N45\_50; Figure 3e). Given a sound  
 244 speed of 1.5 km/s, we select the noise and *T*-wave windows as -45 to -15 s and -15 to 15 s relative  
 245 to the predicted *T*-wave arrivals, respectively. The resulting power spectrum density (PSD) of raw  
 246 OBDAS data exhibits large amplitude noise below 1 Hz, likely associated with ocean-related  
 247 microseisms (Webb, 1998; Figure 4a). The PSD then sharply drops at 1-2 Hz and gradually decays  
 248 from 2 Hz to 40 Hz (Figure 4a), which is consistent with previous observations (Lior et al., 2021;  
 249 Ugalde et al, 2022). The median PSD of the *T*-wave is slightly above the median PSD of noise  
 250 between 4 Hz and 30 Hz, resulting in a low *T*-wave SNR up to ~3 dB at 10-20 Hz (Figure 4). OOI

251 South also exhibits similar  $T$ -wave observations, while the NEPTUNE OBS at a similar water  
 252 depth but a larger distance shows one order of magnitude higher SNRs over a broad frequency  
 253 range (2-40 Hz) peaking at 3-5 Hz (Figure 4b). The low SNRs in OOI OBDAS are due to  
 254 significant noise masking the landward propagating  $T$ -wave. The noise is predominantly grouped  
 255 in the seaward direction with a slowness range of 125-700 m/s, which is likely associated with  
 256 Scholte waves backscattered from a bathymetry step at  $\sim 30$  km on OOI North (Figure 3e). Previous  
 257 OBDAS studies also reported backscattered Scholte waves in ambient noise cross-correlations and  
 258 attributed them to subsurface lateral variations (Spica et al., 2020; Cheng et al., 2021). Here, our  
 259 observations of backscattered Scholte waves are likely linked with the sharp change of bathymetry  
 260 as supported by their consistent presence on both OOI OBDAS arrays (e.g.,  $\sim 30$  km and  $\sim 60$  km  
 261 at OOI South; Figure 3).



262

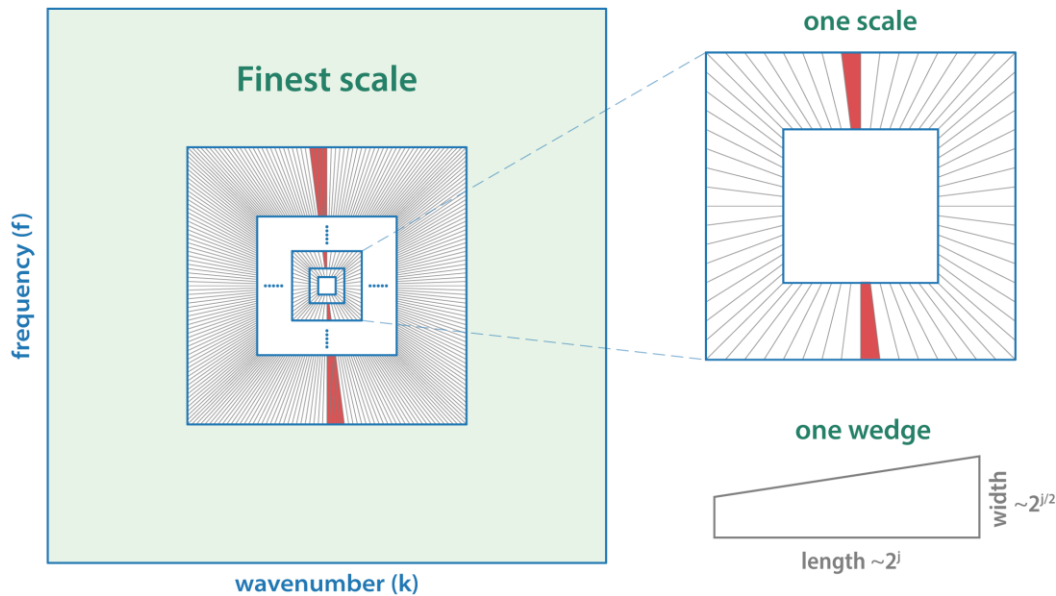
263 **Figure 4.** Power spectral density and SNR of a  $T$ -wave at the OOI OBDAS and a NEPTUNE OBS  
 264 station. (a). Strain rate PSD of raw data and curvelet filtered data at N45\_50. The solid lines denote  
 265 the median PSDs of a  $T$ -wave across N45\_50. The dashed lines correspond to the median PSDs of  
 266 noise. The curves are color-coded to display the outcomes resulting from successive curvelet  
 267 denoising steps. The shadow areas represent the 10th to 90th percentiles of corresponding PSDs  
 268 obtained from individual channels at N45\_50. (b).  $T$ -wave SNRs at OOI North (N45\_50), OOI  
 269 South (S50\_55), and NEPTUNE station NCBC as a function of frequency. The SNR curves plotted  
 270 for OBDAS represent the median SNRs of individual channels. The associated shadow areas  
 271 correspond to the 10th to 90th percentiles of PSDs obtained from individual channels. N45\_50,  
 272 S50\_55, and NCBC are at a similar water depth of  $\sim 400$  m.

273

#### 4.2 Curvelet denoising

274 We adopt a curvelet denoising approach to enhance  $T$ -wave SNRs by taking advantage of  
 275 waveform coherence across dense OBDAS channels. Curvelets are designed to optimally represent  
 276 images with a finite number of geometric discontinuities along twice continuously differentiable  
 277 curves, which is a desirable tool for DAS data with the  $T$ -wave acting as bounded curvature

278 (Candès & Donoho, 2004). Compared to classic Fourier and wavelet transforms, the curvelet  
 279 transform is a tight frame that enables the reconstruction of an image with a series of curvelets  
 280 weighted by their coefficients but is better suited to preserving directional features through a polar  
 281 tiling of the frequency-wavenumber (f-k) domain (Candès et al., 2006). For practical applications  
 282 with discrete data (e.g., OBDAS seismic data), the curvelet transform is usually implemented in a  
 283 discrete frame using Cartesian counterparts of the polar tiling. Explicitly, the f-k plane is  
 284 partitioned into a range of concentric scales dictated by dyadic squares whose width doubles every  
 285 scale (Figure 5). Each scale is further compartmentalized by slowness into a set of parabolic  
 286 angular wedges, which correspond to needle-shaped wave packets or mother curvelets in the time  
 287 domain (Figure 5). Due to the parabolic scaling, the number of wedges doubles every other scale,  
 288 and the mother curvelets consequently become more needle-like at finer scales. In this manner, the  
 289 curvelet transform presents a high degree of localization in position, frequency, and orientation,  
 290 and thus has been exploited in seismology for seismic denoising (Hennenfent & Herrmann, 2006),  
 291 wavefield reconstruction (Jack & Zhan, 2021), and seismic phase augmentation (Yu et al., 2017;  
 292 Zhang & Langston, 2020).

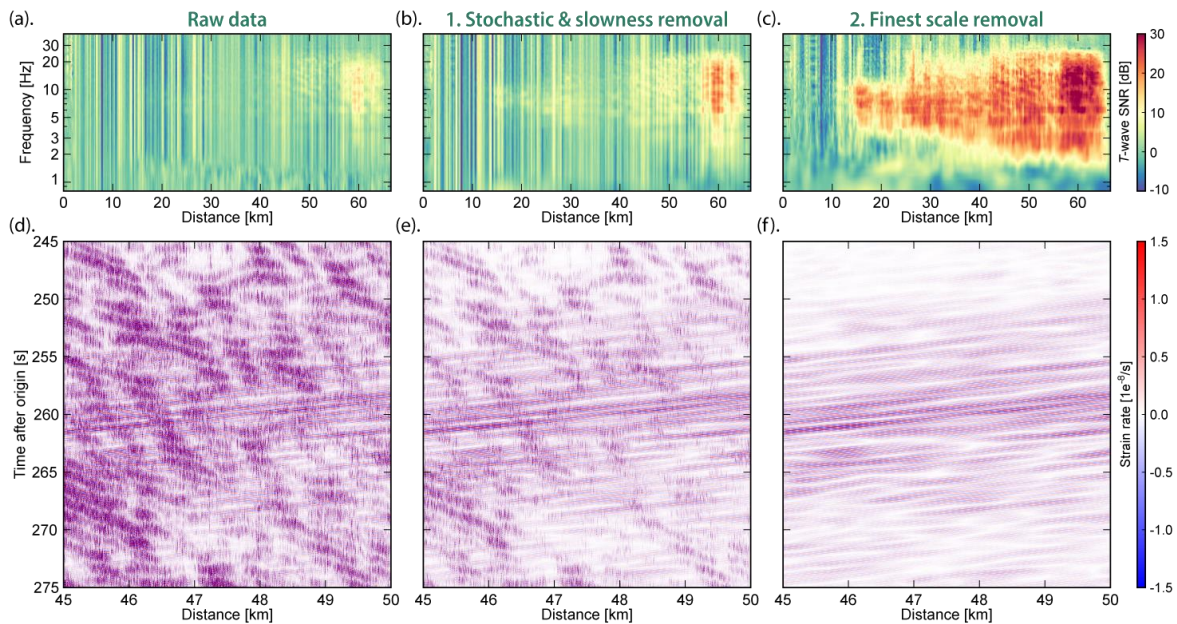


293

294 **Figure 5.** Schematic curvelet tiling of the frequency-wavenumber domain. The right panels are  
 295 examples of the third scale and a parabolic angular wedge. Red wedges denote the wedges  
 296 associated with  $T$ -wave slowness and thus are retained during the slowness removal.

297 Recently, Atterholt et al. (2022) proposed a unified wavefield-partitioning approach for  
 298 simultaneously removing stochastic and coherent noise (e.g., traffic signals) for DAS on land.  
 299 Under the curvelet frame, stochastic noise can be removed by implementing a soft thresholding to  
 300 curvelet coefficients, which involves zeroing the curvelet coefficients below a noise threshold and  
 301 subtracting the threshold from those above it. The effect of slowness removal for coherent noise  
 302 is to mute angular wedges associated with the noise slowness. We follow a similar scheme and

303 apply stochastic and slowness removal to OOI North for the Blanco example. We adopt a  
 304 wrapping-based fast discrete curvelet transform algorithm for computational efficiency and assign  
 305 wavelets to facilitate the implementation of appropriate basis functions at the finest scale (Candès  
 306 et al., 2006). Unlike DAS on land, the noise level and  $T$ -wave energy of OBDAS exhibit significant  
 307 lateral variation dependent on water depth and bathymetry (Figure 3). Therefore, we implement a  
 308 spatially dependent soft thresholding by taking cable location into account. Specifically, we cut a  
 309 180-s window before the  $T$ -wave arrival as a noise window and take the curvelet transform of it.  
 310 For each curvelet, its coefficient matrix describes the corresponding noise level in both temporal  
 311 and spatial dimensions. By rolling along the cable, we set the threshold as the 70th percentile of  
 312 the coefficient matrix at each cable location. In slowness removal, we only retain the curvelets  
 313 associated with  $T$ -waves propagating towards the shore at an apparent speed faster than  $\sim 1.0$  km/s.  
 314 Indeed, the stochastic and slowness removal improves  $T$ -wave SNRs at individual channels and  
 315 suppresses the coherent noise moving seaward (Figures 6a/6d vs 6b/6e). Consequently, the median  
 316 PSD of the stochastic and slowness filtered  $T$ -wave exceeds the noise level at low frequencies (e.g.,  
 317 2-4 Hz; Figure 4a).



318

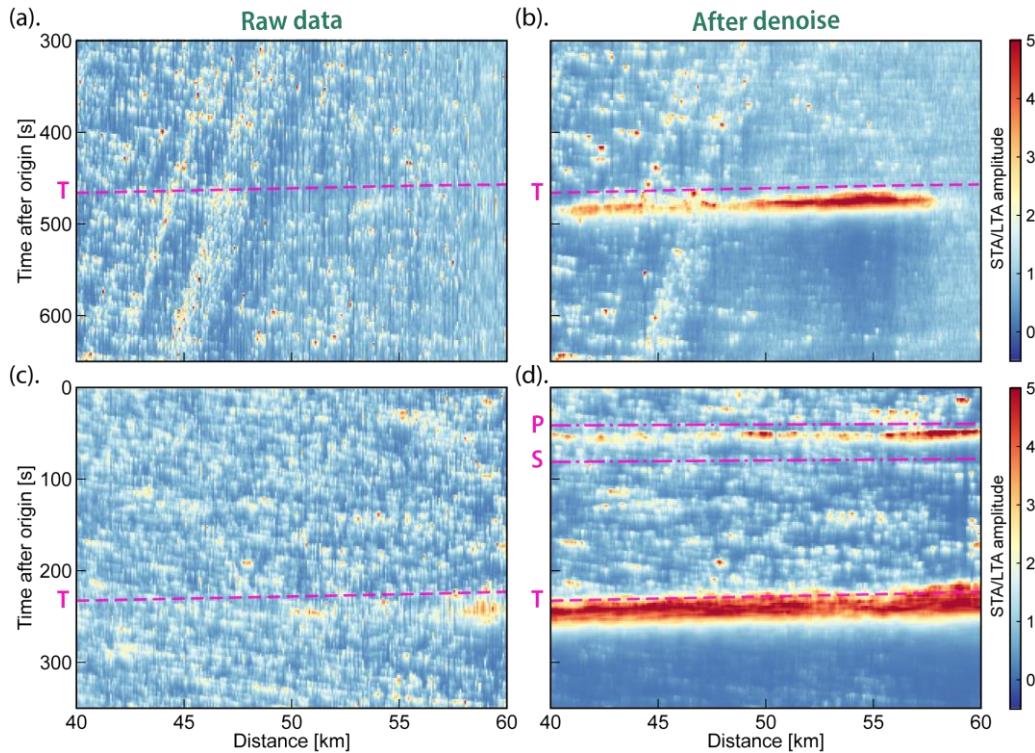
319 **Figure 6.** Illustration of curvelet denoising for enhancing  $T$ -wave SNRs on OBDAS. (a).  $T$ -wave  
 320 SNRs of individual OBDAS channels in OOI North. (b).  $T$ -wave SNRs after stochastic denoising  
 321 and slowness removal. (c).  $T$ -wave SNRs after an additional finest-scale removal. (d). The 4-6 Hz  
 322 OBDAS wavefield at N45\_50 in Figure 3e. (e). The 4-6 Hz OBDAS wavefield after stochastic and  
 323 slowness removal. (f). Similar to (e) but after an additional finest-scale removal.

324 Despite the application of stochastic and slowness denoising, there is certain spiky noise in the  
 325 data that cannot be effectively removed. The spiky noise demonstrates very low coherency and,  
 326 therefore, unlikely corresponds to  $T$ -waves or any natural signals (Figure 6e). Upon thorough  
 327 examination, we find that these spiky artifacts are primarily concentrated in the finest scale of the

328 f-k domain. Thus, to further improve *T*-wave SNRs, we implement an additional finest-scale  
329 removal approach by zeroing out all the coefficients at finest scale (Figures 6c and 6f). As a result,  
330 the median PSD abruptly drops to  $\sim 10^{-19}$ , which is 2-3 orders of magnitude smaller than that of the  
331 original data (Figure 4a). Intriguingly, we observe that a small PSD peak emerges around 20 Hz  
332 in our noise time window, which has been suggested to be associated with whale calls (Wilcock  
333 et al., 2023; Figure 4a). After denoising, the median *T*-wave SNRs of OOI North and OOI South  
334 can reach up to  $\sim 25$  dB over a broad frequency band spanning from 1.5 Hz to 30 Hz, slightly  
335 outperforming a NEPTUNE OBS at a similar water depth (Figure 4b).

### 336 **4.3 Detecting *T*-wave events**

337 Curvelet denoising effectively enhances *T*-wave signals, enabling us to detect small *T*-wave events  
338 hidden in the noises. To illustrate, we select two representative events from the NEPTUNE *T*-wave  
339 catalog (i.e., Event No. 5 and 27 in Table S1). The first event with a small magnitude of ML1.7  
340 occurred near the Explorer ridge, which is about 460 km away from OOI North. The other event  
341 at the Blanco transform fault is at a shorter distance of  $\sim 240$  km. We apply the recursive STA/LTA  
342 algorithm to detect *T*-waves in a frequency band of 5-10 Hz on the 40-60 km segment of OOI  
343 North (N40\_60), which has relatively high SNRs along the cable (Figure 3). However, both events  
344 are too small to produce detectable *T*-wave signals in the raw data. Consequently, the STA/LTA  
345 approach fails to trigger a detection for the *T*-wave (Figures 7a and 7c), except for a small portion  
346 of the cable (e.g., at  $\sim 50$  and  $\sim 60$  km) where STA/LTA amplitudes slightly are higher than the  
347 background levels at the predicted *T*-wave arrival times of the Blanco event (Figure 7c). After  
348 denoising, *T*-waves become evidently visible across N40\_60 for both events (Figures 7b and 7d),  
349 underscoring the great seismic monitoring potential of OBDAS. In addition, curvelet denoising  
350 also substantially enhances the *P*-wave from the Blanco earthquake while the *S*-wave remains  
351 undetected (Figure 7d).



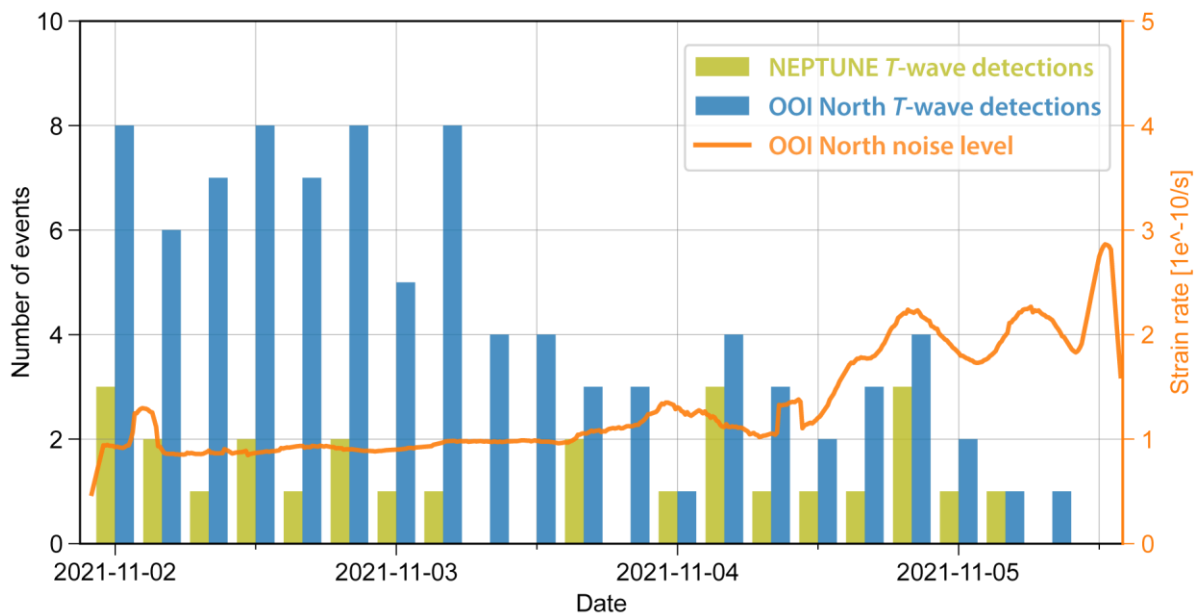
352

353 **Figure 7.** Illustration of curvelet denoising for enhancing  $T$ -wave detectability of OBDAS. (a).  
 354 STA/LTA results for 5-10 Hz raw OBDAS data of the ML1.7 earthquake on November 2nd, 2021  
 355 (Event No. 5 in Table S1). (b). Similar to (a) but for denoised data. (c). STA/LTA detections using  
 356 5-10 Hz raw OBDAS data of the Blanco earthquake on November 5th, 2021 (Event No. 27 in  
 357 Table S1). (d). Similar to (c) but for curvelet denoised data.

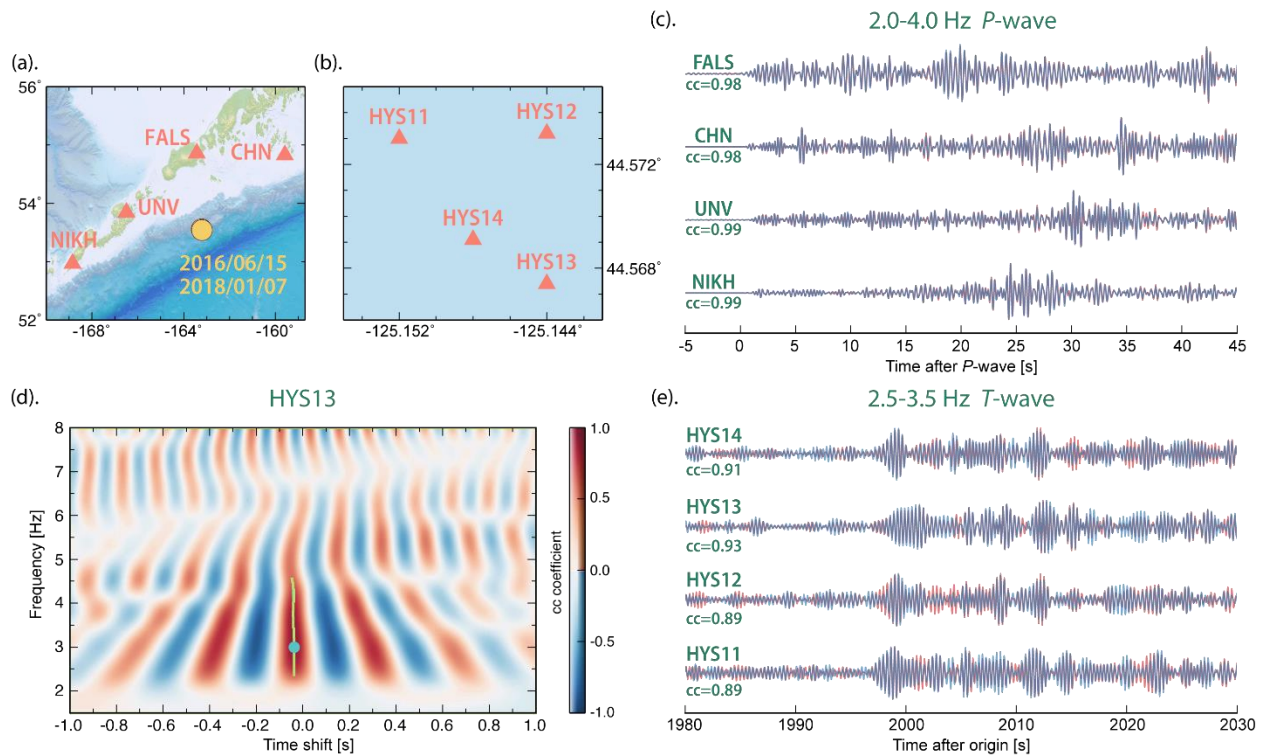
358 The evident effectiveness of curvelet denoising in these two small earthquakes motivates us to  
 359 investigate the potential of OBDAS for long-term  $T$ -wave detection. We use the complete 4-day  
 360 dataset of N40\_60, downsample the data to 50 Hz, divide them into 10-min windows, and apply  
 361 curvelet denoising and recursive STA/LTA. We average the STA/LTA over all channels with a  
 362 slowness correction of 1.5 km/s. An event is detected if the averaged STA/LTA amplitude exceeds  
 363 a threshold of 1.5, similar to the NEPTUNE  $T$ -wave catalog. After visual scrutinization to remove  
 364  $P$ -waves and false detections, we document a total of 92  $T$ -wave events for OOI North. Compared  
 365 to the NEPTUNE  $T$ -wave catalog, our new OOI North  $T$ -wave catalog includes 17 of the 27  
 366 NEPTUNE events. The missed 10 events are local seismicity near the NEPTUNE array (gray  
 367 circles in Figure 2), which are probably too small to be detected at OOI North. Meanwhile, OOI  
 368 North identifies 2-3 times more earthquakes than the NEPTUNE array in the first half of the  
 369 experiment (Figure 8). The excess  $T$ -wave events on OOI North are likely associated with  
 370 aftershocks of a mb3.9 Blanco earthquake that occurred on November 1<sup>st</sup>, 2021, at 06:15:19 UTC,  
 371 right before the experiment. The  $T$ -wave detection rate of OOI North gradually decreases from 6-  
 372 8 events per 4 hours on November 2<sup>nd</sup> to 1-4 events per 4 hours on November 4<sup>th</sup> and 5<sup>th</sup>. This  
 373 declining trend could be partially attributed to an increase in the noise level starting on November

374 4<sup>th</sup> (Figure 8). A likely decrease in aftershock productivity may also contribute to the reduced  
 375 detections but we lack independent observations to support this interpretation.

376 The significantly higher number of *T*-wave event detections on OOI North compared to the  
 377 NEPTUNE network highlights the potential of OBDAS for long-term marine seismicity  
 378 monitoring, though the comparison may be not entirely fair given their different instrument  
 379 locations. In spite of large uncertainty, a straightforward linear extrapolation based on the 92  
 380 detections observed over a 4-day period suggests a potential annual detection rate of approximately  
 381 8000 events. Using U.S. Navy SOSUS hydrophones, Fox et al. (1993) reported an annual detection  
 382 of 1000-2000 events in the Juan de Fuca region and established a Gutenberg-Richter law with a *b*-  
 383 value of 1.42. Based on their model, our extrapolation of ~8000 events per year implies that OOI  
 384 OBDAS can detect regional seismicity with a minimum magnitude of *mb*1.4.



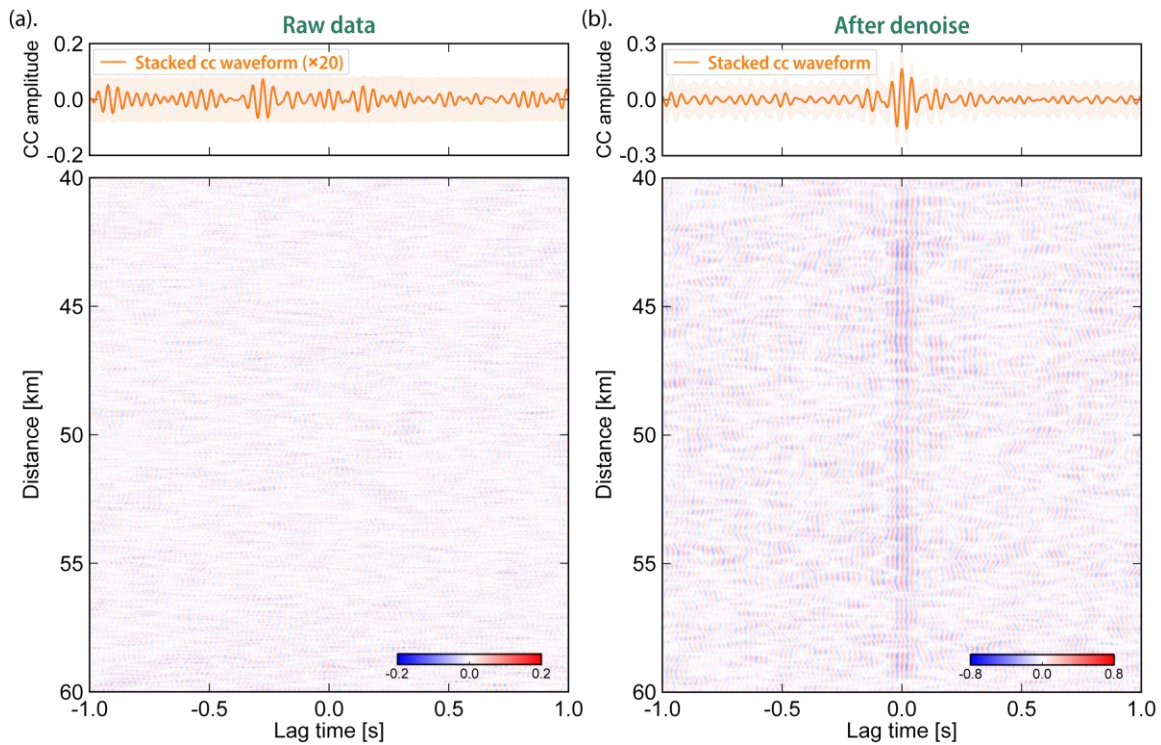
398 previous observations in the Indian Ocean (Callies et al., 2023; Wu et al., 2023). Taking a CC  
 399 coefficient threshold of 0.6, the  $T$ -wave travel time shifts between 2.35 Hz and 4.6 Hz would be  
 400 used to infer average ocean temperature change along the  $T$ -wave path. In this example, the slight  
 401  $T$ -wave travel time shift of -0.04 s at 3 Hz (Figure 9d) indicates a weakly warming ocean averaged  
 402 over the top 3 km of the water column along the  $\sim 3000$  km source-receiver path (see supplementary  
 403 text S2 and Figure S2 for more details; Komatitsch & Tromp, 1999; McDougall & Barker, 2011;  
 404 Forget et al., 2015).



405  
 406 **Figure 9.** Illustration of SOT concept using repeating earthquakes in the Aleutian trench and OOI  
 407 OBSs. (a). The map of repeating earthquakes and local stations at the Aleutian trench. (b). The  
 408 map of OOI OBS array. (c).  $P$ -waves of the 15 June 2016 event (red) and 7 January 2018 (blue)  
 409 event. The station names and CC coefficients are indicated on the left.  $P$ -waves from the 2016  
 410 event are synchronized based on their predicted arrivals at each station using the ISC source  
 411 parameters. The  $P$ -waves from the 2018 event are aligned with the corresponding 2016  $P$ -waves  
 412 using waveform cross correlation. (d). Frequency dependent  $T$ -wave CC results of HYS13. The  
 413 green line indicates the frequency-dependent time shifts measured by tracking the stripe of peak  
 414 CC coefficient above 0.6. The green dot shows a time shift of -0.04 s measured at 3 Hz. (e).  $T$ -  
 415 waves at the four OOI OBSs. The relative origin time error between the 2016 event and 2018 event  
 416 is corrected using the  $P$ -waves shown in (c).

417 Within the limited 4-day experiment period, we do not find any natural repeating earthquake pair  
 418 in the Northeast Pacific region producing  $T$ -waves usable for SOT. Thus, we generate pseudo-  
 419 repeating earthquakes to evaluate the SOT performance of OBDAS by incorporating realistic noise

420 data into the  $T$ -waves of the Mw5.2 Fox Islands earthquake. Specifically, we randomly select 20  
 421 three-minute noise data segments from OOI North and superimpose each of these noise segments  
 422 onto magnitude-calibrated  $T$ -waves. To perform the calibration, we assume a circular crack model  
 423 and constant stress drop (Madariaga, 1976; Allmann & Shearer, 2009). Based on this assumption,  
 424 the  $T$ -wave amplitude would be proportional to  $M_0^{2/3}$ , where  $M_0$  represents the seismic moment.  
 425 For instance, a decrease in the moment magnitude by one-unit results in a 10-fold drop of  $T$ -wave  
 426 amplitude. With the scaling, we generate pseudo-repeating OBSDAS  $T$ -waves for a given  
 427 magnitude, perform curvelet denoising, and evaluate the performance of OBSDAS for SOT. We  
 428 use the OBSDAS data at N40\_60 for illustration. It is important to point out that applying stochastic  
 429 removal independently to each pseudo-repeating event can lead to inconsistent zeroing of noisy  
 430 curvelet coefficients and compromise the accuracy of  $T$ -wave time shifts. To ensure a consistent  
 431 and unbiased treatment of the repeating  $T$ -waves, we identify and remove the overlapping noisy  
 432 curvelet coefficients for each given pair in the curvelet denoising.



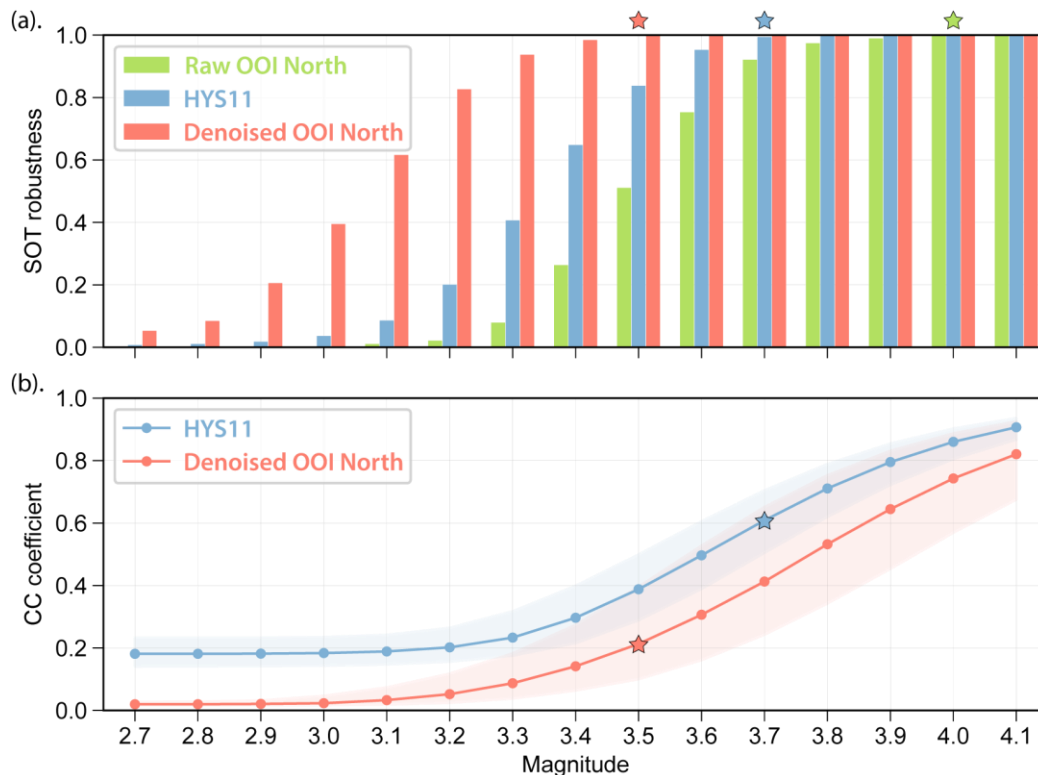
433

434 **Figure 10.** Illustration of improved CCs with curvelet denoising of OBSDAS Data. (a). Raw  $T$ -  
 435 wave CCs between two Mw3.5 pseudo-repeating earthquakes at 3-5 Hz. The top panel presents  
 436 the stacked CC (multiplied by 20 for better visualization), the orange shadow area denotes the  
 437 10th-90th percentile of individual CCs. (b). Similar to (a) but for denoised  $T$ -waves.

438 As an example, we generate two M3.5 pseudo-repeating earthquakes by downscaling the  $T$ -waves  
 439 from the Mw5.2 Fox Islands earthquake with a factor of 50. We cut the two repeating  $T$ -waves  
 440 with a 60-s time window and cross correlate them at individual OBSDAS channels. However, the  
 441  $T$ -wave signals are so weak relative to the noise that no coherent CC signals are observed (Figure

442 10a). The stacked CC waveform exhibits a weak peak at a time shift of -0.27 s, substantially  
 443 deviating from the input value of 0.0 s. In contrast, curvelet denoising greatly enhances the *T*-wave,  
 444 resulting in coherent CC signals that are visible on most channels. The coherent signal is further  
 445 enhanced in the stacked CC waveform with a clear peak amplitude at 0.0 s, matching the expected  
 446 input number (Figure 10b). Here, we first cross correlate individual *T*-waves and subsequently  
 447 stack the resulting CCs to accommodate potential waveform variations among different channels.  
 448 Conversely, stacking array waveforms prior to the cross-correlation step may lead to destructive  
 449 interference of *T*-waves, compromising the accuracy of the measurements.

450 To ensure robustness, we repeat this M3.5 repeater analysis using all the selected 20 noise windows,  
 451 which yields a total of 190 pseudo-repeating earthquake pairs. We successfully retrieve the  
 452 expected time shift of 0.00 s across all pairs, with an error margin of less than 0.02 s corresponding  
 453 to our downsampled time interval (Figure 11a). Furthermore, we extend the M3.5 scenario to a  
 454 wide range of earthquake magnitude, spanning from M2.7 to M4.1 with an interval of M0.1.  
 455 Curvelet denoising evidently reduces the magnitude required for reliable time shift measurements  
 456 (Figure 11a). Taking a criterion of >99% pairs with successful time shift retrieval (i.e., SOT  
 457 robustness >0.99 in Figure 11a), the magnitude threshold decreases from M4.0 to M3.5. Based on  
 458 the Gutenberg-Richter law (Gutenberg & Richter, 1944), a decrease in magnitude threshold by  
 459 M0.5 would result in a roughly threefold increase in the count of usable repeating events.  
 460 Additionally, the quadratic relationship between the number of repeaters and repeating pairs  
 461 indicates a potential order of magnitude increase of repeating pairs.



463 **Figure 11.** Comparison of SOT performance between OBDAS and OBS. (a). SOT robustness  
464 using HYS11 data, raw OOI North data, and denoised OOI North data, as a function of earthquake  
465 magnitude. The SOT robustness is indexed by the ratio of successful pairs, where the input travel  
466 time shift of 0.00 s is accurately recovered, to the total number of repeating pairs. The stars indicate  
467 magnitude thresholds, above which >99% pairs accurately retrieve the time shift. (b). CC peak  
468 amplitudes using HYS11 and denoised OOI North data, as a function of earthquake magnitude.  
469 The blue represents the median of CC peak amplitudes among the 1400 repeating pairs for HYS11.  
470 The red line shows the median of stacking cCC amplitude peaks among the 190 repeating pairs for  
471 OOI North. The shadow area indicates the 10th-90th percentiles.

472 We also attempt to evaluate the SOT performance of a neighboring OBS station, specifically  
473 HYS11, for a comparison with OBDAS (Figure 1). However, during the community experiment,  
474 HYS11 was inactive for maintenance and did not record the *T*-wave from the M5.2 Fox island  
475 earthquake. To address the issue, one could involve another M5.2 earthquake recorded by HYS11  
476 or a different magnitude earthquake with magnitude calibration. However, such an approach can  
477 introduce substantial uncertainty due to the complex nature of *T*-wave excitation, where even slight  
478 differences in source parameters can affect *T*-wave amplitudes and thus lead to calibration biases.  
479 Therefore, we opt not to solely rely on the simplistic calibration method. Alternatively, we leverage  
480 the NEPTUNE dataset, which captures earthquakes during, after and prior to the experiment, to  
481 establish a reliable calibration relation between OBDAS and HYS11 (see supplement material text  
482 S3 for details; Figure S3). Using NEPTUNE as a reference, the calibration method effectively  
483 cancels out complex effects arising from differences in source parameters and bridges a direct  
484 comparison between OBS and OBDAS. Similar to the aforementioned evaluation for OBDAS, we  
485 generate pseudo-repeating pairs for HYS11 by utilizing seven Mw5.0+ Fox islands earthquakes  
486 (Figure S4) and 200 randomly selected noise waveforms. With a total of 1400 pseudo-repeating  
487 pairs, the magnitude threshold for HYS11 is M3.7, higher than the threshold of M3.5 for OBDAS  
488 (Figure 11a). This magnitude difference indicates that using OBDAS can potentially provide four  
489 times more small repeating pairs for SOT compared to OBS. However, it is important to note that  
490 our comparison is influenced by the noise level of OBDAS. The current 4-day OBDAS data show  
491 large variations in noise levels (Figure 8), indicating that long-term OBDAS observations are  
492 required for a robust quantification. In addition, our estimated magnitude threshold for SOT can  
493 vary substantially depending on the region and the earthquake source parameters, as *T*-wave  
494 excitation is strongly modulated by bathymetric features in different regions, resulting in varying  
495 SNRs of the *T*-wave (de Groot-Hedlin & Orcutt, 2001).

496 In practical SOT applications, a CC coefficient threshold is typically used to ensure accurate *T*-  
497 wave time shift measurements. Previous studies using *T*-wave stations and hydrophones have  
498 established an empirical threshold of 0.6 based on visual examination of the CC waveforms,  
499 lacking a solid justification (Wu et al., 2020). Intriguingly, our pseudo-repeating tests show that  
500 the median of CC peak amplitudes for HYS11 corresponds to 0.6 at the magnitude threshold of

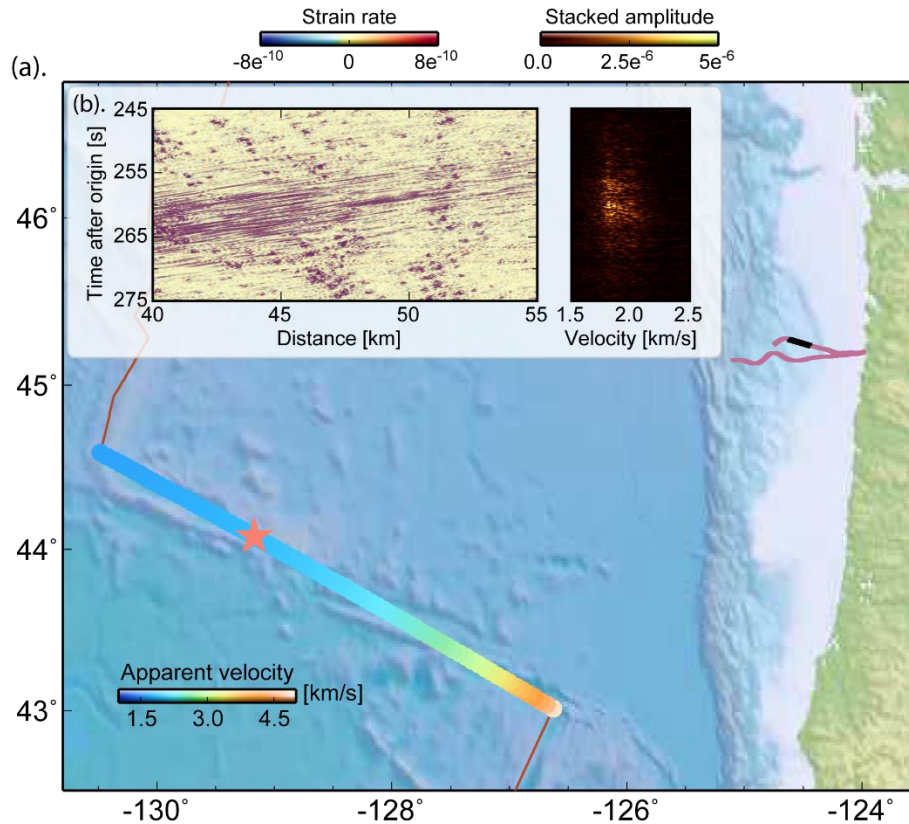
501 M3.7 (Figure 11b), supporting the previous choices. For OBDAS data, a lower threshold, such as  
502 0.2 for OOI North, can be adopted benefiting from stacking of multiple channels.

## 503 **6 Discussion**

504 In previous sections, we demonstrated the potential of OBDAS in detecting *T*-wave events and  
505 monitoring large-scale ocean temperature changes. However, due to the limited 4-day data and  
506 confined azimuthal coverage of OBDAS, certain questions remain unanswered. For instance, the  
507 locations of detected *T*-wave events are unexplored, and the performance of OBDAS for SOT can  
508 be influenced by varying noise sources across time and space. In the following section, we discuss  
509 these issues under the context of future investigation, when more OBDAS data become accessible.

### 510 **6.1 Locating earthquakes using OBDAS *T*-waves**

511 Even though retrieving a complete source location from *T*-waves recorded at one site is  
512 challenging, the use of array beamforming enables us to estimate the source azimuth with OBDAS.  
513 For instance, the theoretical *T*-wave arrival times from Blanco earthquakes unveil a discernible  
514 pattern of location-dependent apparent velocity (Figures 12 and S5). For *T*-waves on the N40\_55  
515 segment, its apparent velocity gradually increases from 1.5 km/s to 5 km/s as an earthquake moves  
516 eastward along the Blanco transform fault (Figure 12), allowing for source azimuth estimation.  
517 Taking a Blanco event that occurred at 00:05 on November 2<sup>nd</sup>, 2021, as an example, a slant stack  
518 of its *T*-waves at N40\_55 exhibits an amplitude peak at an apparent velocity of 1.82 km/s, which  
519 corresponds to a back azimuth of 252° given a propagation speed of 1.5 km/s. The resolved back  
520 azimuth intercepts the Blanco fault trace at a location of 44.08°N, 129.17°W. With this location,  
521 we calculate the theoretical *T*-wave arrival times at two NEPTUNE stations, which align  
522 reasonably well with observed data (Figure S6). However, only OOI North is used in this example,  
523 leaving the epicenter distance unresolved. Looking forward, an optimal approach would involve  
524 integrating travel time and slowness data from all available instruments, including OBDAS, *T*-  
525 wave stations, and hydrophones from a wide range of azimuths.



526

527 **Figure 12.** Locating the 2021-11-02T00:05 Blanco earthquake using *T*-waves on OOI North. (a).  
 528 Slowness sensitivity of OOI North *T*-wave to earthquake location. The color along the Blanco  
 529 transform fault shows predicted *T*-wave slowness at N40\_55 (black line), corresponding to  
 530 different earthquake locations along the fault. The red star denotes the estimated location of the  
 531 2021-11-02T00:05 event. (b). *T*-waves at 5-10 Hz and slant stack results.

## 532 6.2 Noise in OBDAS data

533 The noise level in OBDAS data is a critical parameter affecting the *T*-wave data quality. During  
 534 the four-day experiment, the OBDAS noise level gradually increased by a factor of 1-2. The source  
 535 of OBDAS noise and its temporal variability remain unclear. Analysis of previous OBS data  
 536 indicates that tilt and compliance processes are major contributors to OBS noise, both of which  
 537 are associated with ocean dynamics (Hilmo & Wilcock, 2020; Janiszewski et al., 2022). While  
 538 OBDAS and OBS operate on distinct principles for vibration sensing, their noise sources are not  
 539 necessarily identical. Nevertheless, we do observe fluctuations in ocean wave height and wind  
 540 direction within the four-day period (Hersbach et al., 2023), suggesting a potential link between  
 541 OBDAS noise and ocean dynamics (Figure S7). However, such correlation is still inconclusive  
 542 due to limited 4-day data.

543 To evaluate the effect of varying noise on SOT, we randomly select 20 noise samples each from  
 544 the first and last 24 hours, representing low and high noise levels, respectively. Consequently, the

545 magnitude threshold for high-quality SOT increases from M3.2 at low noise level to M3.6 at high  
546 noise level (Figure S8a). Nonetheless, the corresponding median of CC peak amplitudes for both  
547 scenarios consistently fall within the range of 0.1-0.2, reinforcing that a CC coefficient threshold  
548 of 0.2 could be suitable for SOT using a 20-km OBDAS cable regardless of noise level (Figure  
549 S8b). Meanwhile, in previous sections, we use a fixed threshold of 70th percentile noise level for  
550 the stochastic removal. Given the temporal variability of OBDAS noise levels, one may adjust the  
551 threshold for better denoising. Yet, our tests indicate that varying the threshold within the 50th-  
552 100th percentile range barely affects the SOT performance – only the 90th percentile threshold  
553 case marginally outperforms the others (Figure S9). However, our assessment strongly relies on  
554 current dataset and might not be generalized to other OBDAS datasets.

555 Although curvelet denoising efficiently reduces noise, the exact sources of the noise remain  
556 unknown. In particular, the strong incoherent spiky noise is ubiquitous in the OBDAS data (Figure  
557 S10). It often accompanies ocean gravity waves and becomes most pronounced around the peaks  
558 and troughs of these waves (Figure S10). Its amplitude generally increases at shallower water  
559 depths (Figure S10). Intriguingly, higher noise levels in shallower water have also been reported  
560 in OBS data, which are attributed to the seafloor compliance effects due to orbital motions of ocean  
561 waves (Hilmo & Wilcock, 2020; Janiszewski et al., 2022). The spiky noise in OBDAS data also  
562 shows a similar depth dependency, although its exact mechanism remains mysterious. Thus,  
563 further investigations with more data from diverse ocean environments are warranted to better  
564 understand the characteristics and sources of OBDAS noise.

## 565 **7 Conclusions**

566 In this study, we investigate the performance of OBDAS for *T*-wave detection and SOT using the  
567 4-day data collected from the OOI cables offshore central Oregon. We develop a curvelet  
568 denoising that effectively enhances *T*-wave signals while mitigating noises. This scheme includes  
569 stochastic noise removal, slowness removal and finest-scale removal. Our results demonstrate that  
570 curvelet denoising effectively enhances *T*-wave signal, resulting in a substantial improvement of  
571 *T*-wave detectability. After denoising, we identify 92 *T*-wave events on OOI North, which is three  
572 times more than the NEPTUNE catalog. However, the *T*-wave detectability of OOI North  
573 decreases due to a higher noise level during the latter half of the experiment, highlighting the  
574 influences of noise variations. We also evaluate the SOT feasibility of OBDAS and juxtapose its  
575 performance with conventional OBSs. To evaluate the feasibility, we synthesize *T*-waves of  
576 pseudo-repeating earthquakes using the observed *T*-waves from a Mw5.2 Fox Islands earthquake  
577 and background noises recorded by OOI OBDAS. Our findings show that OOI OBDAS,  
578 leveraging its array data advantage, can record *T*-waves from a ~3000 km distant repeating  
579 earthquake, with a magnitude >M3.5, suitable for SOT. In contrast, using OBS requires a slightly  
580 higher magnitude threshold of M3.7. However, the performance of OBDAS for *T*-wave detection

581 and SOT highly depends on both natural and instrumental noise levels, which awaits further  
582 investigation.

583

#### 584 **Acknowledgments**

585 We are grateful for the constructive discussions with Daniel Lizarralde and John A Collins. This  
586 project is supported by the Woods Hole Oceanographic Institution Independent Research &  
587 Development Program. We thank the high-performance computing resources at Woods Hole  
588 Oceanographic Institution made available for conducting this research. Z. S. also acknowledges  
589 the support of the Weston Howland Jr. Postdoctoral Scholarship.

#### 590 **Open Research**

591 The curvelet code is available on the curvelet.org website (<http://www.curvelet.org>) and  
592 <https://github.com/atterholt/curvelet-denoising>. The OOI RCA community experiment OBDAS data is available  
593 from <http://piweb.ooirsn.uw.edu/das/>. The ocean wave height and wind speed data are downloaded from  
594 Copernicus Climate Change Service Climate Data Store ([10.24381/cds.adbb2d47](https://doi.org/10.24381/cds.adbb2d47)).

595 **References**

- 596 Allmann, B. P., & Shearer, P. M. (2009). Global variations of stress drop for moderate to large  
597 earthquakes. *Journal of Geophysical Research: Solid Earth*, 114(B1).
- 598 ATOC Consortium. (1998). Ocean climate change: Comparison of acoustic tomography, satellite  
599 altimetry, and modeling. *Science*, 281(5381), 1327-1332.
- 600 Atterholt, J., Zhan, Z., Shen, Z., & Li, Z. (2022). A unified wavefield-partitioning approach for  
601 distributed acoustic sensing. *Geophysical Journal International*, 228(2), 1410-1418.
- 602 Bakun, W. H., & Joyner, W. B. (1984). The ML scale in central California. *Bulletin of the*  
603 *Seismological Society of America*, 74(5), 1827-1843.
- 604 Barnes, C. R., Best, M. M., & Zielinski, A. (2008). The NEPTUNE Canada regional cabled ocean  
605 observatory. *Technology (Crayford, England)*, 50(3).
- 606 Bondár, I., & Storchak, D. A., (2011). Improved location procedures at the International  
607 Seismological Centre. *Geophys. J. Int.*, 186, 1220-1244
- 608 Buehler, J. S., & Shearer, P. M. (2015). T phase observations in global seismogram  
609 stacks. *Geophysical Research Letters*, 42(16), 6607-6613.
- 610 Callies, J., Wu, W., Peng, S., & Zhan, Z. (2023). Vertical-Slice Ocean Tomography With Seismic  
611 Waves. *Geophysical Research Letters*, 50(8), e2023GL102881.
- 612 Candès, E., & Donoho, D. L. (2004). New tight frames of curvelets and optimal representations of  
613 objects with piecewise C2 singularities. *Communications on Pure and Applied Mathematics: A*  
614 *Journal Issued by the Courant Institute of Mathematical Sciences*, 57(2), 219-266.
- 615 Candès, E., Demanet, L., Donoho, D., & Ying, L. (2006). Fast discrete curvelet  
616 transforms. *multiscale modeling & simulation*, 5(3), 861-899.
- 617 Cheng, F., Chi, B., Lindsey, N. J., Dawe, T. C., & Ajo-Franklin, J. B. (2021). Utilizing distributed  
618 acoustic sensing and ocean bottom fiber optic cables for submarine structural  
619 characterization. *Scientific reports*, 11(1), 1-14
- 620 Collins, M.P. (1936). *Bulletin Number 5*. Harvard University Seismograph Station, 23.
- 621 Das, R., Wason, H. R., & Sharma, M. L. (2011). Global regression relations for conversion of  
622 surface wave and body wave magnitudes to moment magnitude. *Natural hazards*, 59, 801-810.
- 623 de Groot-Hedlin, C. D. (2005). Estimation of the rupture length and velocity of the Great Sumatra  
624 earthquake of Dec 26, 2004 using hydroacoustic signals. *Geophysical Research Letters*, 32(11).
- 625 de Groot-Hedlin, C. D., & Orcutt, J. A. (2001). Excitation of T-phases by seafloor scattering. *The*  
626 *Journal of the Acoustical Society of America*, 109(5), 1944-1954.
- 627 Dziak, R. P., Bohnenstiehl, D. R., Matsumoto, H., Fox, C. G., Smith, D. K., Tolstoy, M., ... &  
628 Fowler, M. J. (2004). P-and T-wave detection thresholds, Pn velocity estimate, and detection of  
629 lower mantle and core P-waves on ocean sound-channel hydrophones at the Mid-Atlantic  
630 Ridge. *Bulletin of the Seismological Society of America*, 94(2), 665-677.
- 631 Dziak, R. P., Bohnenstiehl, D. R., & Smith, D. K. (2012). Hydroacoustic monitoring of oceanic  
632 spreading centers: Past, present, and future. *Oceanography*, 25(1), 116-127.

- 633 Fang, J., Yang, Y., Shen, Z., Biondi, E., Wang, X., Williams, E. F., ... & Zhan, Z. (2023).  
634 Directional Sensitivity of DAS and Its Effect on Rayleigh-Wave Tomography: A Case Study in  
635 Oxnard, California. *Seismological Society of America*, 94(2A), 887-897.
- 636 Forget, G. A. E. L., Campin, J. M., Heimbach, P., Hill, C. N., Ponte, R. M., & Wunsch, C. (2015).  
637 ECCO version 4: An integrated framework for non-linear inverse modeling and global ocean state  
638 estimation. *Geoscientific Model Development*, 8(10), 3071-3104.
- 639 Fox, C. G., Dziak, R. P., Matsumoto, H., & Schreiner, A. E. (1993). Potential for monitoring low-  
640 level seismicity on the Juan-de-Fuca ridge using military hydrophone arrays. *Marine Technology*  
641 *Society Journal*, 27(4), 22-30.
- 642 Fox, C. G., Radford, W. E., Dziak, R. P., Lau, T. K., Matsumoto, H., & Schreiner, A. E. (1995).  
643 Acoustic detection of a seafloor spreading episode on the Juan de Fuca Ridge using military  
644 hydrophone arrays. *Geophysical Research Letters*, 22(2), 131-134.
- 645 Fox, C. G., Matsumoto, H., & Lau, T. K. A. (2001). Monitoring Pacific Ocean seismicity from an  
646 autonomous hydrophone array. *Journal of Geophysical Research: Solid Earth*, 106(B3), 4183-  
647 4206.
- 648 Gutenberg, B., & Richter, C. F. (1944). Frequency of earthquakes in California. *Bulletin of the*  
649 *Seismological society of America*, 34(4), 185-188.
- 650 Hamada, N. (1985). T waves recorded by ocean bottom seismographs off the south coast of Tokai  
651 area, central Honshu, Japan. *Journal of Physics of the Earth*, 33(5), 391-410.
- 652 Hanson, J. A., & Bowman, J. R. (2006). Methods for monitoring hydroacoustic events using direct  
653 and reflected T waves in the Indian Ocean. *Journal of Geophysical Research: Solid Earth*, 111(B2)
- 654 Hartog, A. H. (2017). *An introduction to distributed optical fibre sensors*. CRC press.
- 655 Hennenfent, G., & Herrmann, F. J. (2006). Seismic denoising with nonuniformly sampled  
656 curvelets. *Computing in Science & Engineering*, 8(3), 16-25.
- 657 Hersbach, H., Bell, B., Berrisford, P., Biavati, G., Horányi, A., Muñoz Sabater, J., ... & Thépaut,  
658 J. N. (2023). ERA5 hourly data on single levels from 1940 to present. *Copernicus Climate Change*  
659 *Service (C3S) Climate Data Store (CDS)*. 10.24381/cds.adbb2d47 (Accessed on 08-Aug-2023)
- 660 Hilmo, R., & Wilcock, W. S. (2020). Physical sources of high-frequency seismic noise on Cascadia  
661 Initiative ocean bottom seismometers. *Geochemistry, Geophysics, Geosystems*, 21(10),  
662 e2020GC009085.
- 663 Ide, S., Araki, E., & Matsumoto, H. (2021). Very broadband strain-rate measurements along a  
664 submarine fiber-optic cable off Cape Muroto, Nankai subduction zone, Japan. *Earth, Planets and*  
665 *Space*, 73(1), 1-10
- 666 Jaggard, T. A. (1930). How the seismograph works. *The Volcano Letter*, 268, 1-4.
- 667 Janiszewski, H. A., Eilon, Z., Russell, J. B., Brunsvik, B., Gaherty, J. B., Mosher, S. G., ... & Coats,  
668 S. (2023). Broad-band ocean bottom seismometer noise properties. *Geophysical Journal*  
669 *International*, 233(1), 297-315.
- 670 Kelley, D. S., Delaney, J. R., & Juniper, S. K. (2014). Establishing a new era of submarine volcanic  
671 observatories: Cabling Axial Seamount and the Endeavour Segment of the Juan de Fuca  
672 Ridge. *Marine Geology*, 352, 426-450.

- 673 Kennett, B. L. N., & Engdahl, E. R. (1991). Traveltimes for global earthquake location and phase  
674 identification. *Geophysical Journal International*, 105(2), 429-465.
- 675 Komatitsch, D., & Tromp, J. (1999). Introduction to the spectral element method for three-  
676 dimensional seismic wave propagation. *Geophysical journal international*, 139(3), 806-  
677 822. Koyanagi, S., Aki, K., Biswas, N., & Mayeda, K. (1995). Inferred attenuation from site effect-  
678 corrected T phases recorded on the island of Hawaii. *Pure and Applied Geophysics*, 144(1), 1-17.
- 679 Li, Z., Shen, Z., Yang, Y., Williams, E., Wang, X., & Zhan, Z. (2021). Rapid response to the 2019  
680 Ridgecrest earthquake with distributed acoustic sensing. *AGU Advances*, 2(2), e2021AV000395.
- 681 Lindsey, N. J., Dawe, T. C., & Ajo-Franklin, J. B. (2019). Illuminating seafloor faults and ocean  
682 dynamics with dark fiber distributed acoustic sensing. *Science*, 366(6469), 1103-1107.
- 683 Lindsey, N. J., & Martin, E. R. (2021). Fiber-optic seismology. *Annual Review of Earth and*  
684 *Planetary Sciences*, 49, 309-336.
- 685 Linehan, D. (1940). Earthquakes in the West Indian region. *Eos, Transactions American*  
686 *Geophysical Union*, 21(2), 229-232.
- 687 Lior, I., Sladen, A., Rivet, D., Ampuero, J. P., Hello, Y., Becerril, C., ... & Markou, C. (2021). On  
688 the detection capabilities of underwater distributed acoustic sensing. *Journal of Geophysical*  
689 *Research: Solid Earth*, 126(3), e2020JB020925.
- 690 Madariaga, R. (1976). Dynamics of an expanding circular fault. *Bulletin of the Seismological*  
691 *Society of America*, 66(3), 639-666.
- 692 Martin, E. R., Lindsey, N. J., Ajo-Franklin, J. B., & Biondi, B. L. (2021). Introduction to  
693 interferometry of fiber-optic strain measurements. *Distributed Acoustic Sensing in Geophysics:*  
694 *Methods and Applications*, 111-129.
- 695 Matsumoto, H., Araki, E., Kimura, T., Fujie, G., Shiraishi, K., Tonegawa, T., ... & Karrenbach, M.  
696 (2021). Detection of hydroacoustic signals on a fiber-optic submarine cable. *Scientific*  
697 *reports*, 11(1), 1-12.
- 698 Matsumoto, H., Haralabus, G., Zampolli, M., & Özel, N. M. (2016). T-phase and tsunami pressure  
699 waveforms recorded by near-source IMS water-column hydrophone triplets during the 2015 Chile  
700 earthquake. *Geophysical Research Letters*, 43(24), 12-511.
- 701 McDougall, T. J., & Barker, P. M. (2011). Getting started with TEOS-10 and the Gibbs Seawater  
702 (GSW) oceanographic toolbox. *Scor/Iapso WG*, 127(532), 1-28.
- 703 Muir, J. B., & Zhan, Z. (2021). Seismic wavefield reconstruction using a pre-conditioned wavelet-  
704 curvelet compressive sensing approach. *Geophysical Journal International*, 227(1), 303-315.
- 705 Munk, W. H., Spindel, R. C., Baggeroer, A., & Birdsall, T. G. (1994). The heard island feasibility  
706 test. *The Journal of the Acoustical Society of America*, 96(4), 2330-2342
- 707 Munk, W., & Wunsch, C. (1979). Ocean acoustic tomography: A scheme for large scale  
708 monitoring. *Deep Sea Research Part A. Oceanographic Research Papers*, 26(2), 123-161
- 709 Okal, E. A. (2001). "Detached" deep earthquakes: are they really? *Physics of the Earth and*  
710 *Planetary Interiors*, 127(1-4), 109-143.
- 711 Okal, E. A. (2008). The generation of T waves by earthquakes. *Advances in Geophysics*, 49, 1-6

- 712 Okal, E. A., & Talandier, J. (1986). T-wave duration, magnitudes and seismic moment of an  
713 earthquake-application to tsunami warning. *Journal of Physics of the Earth*, 34(1), 19-42.
- 714 Parnell-Turner, R., Smith, D. K., & Dziak, R. P. (2022). Hydroacoustic monitoring of seafloor  
715 spreading and transform faulting in the equatorial Atlantic Ocean. *Journal of Geophysical*  
716 *Research: Solid Earth*, 127(7), e2022JB024008.
- 717 Riser, S. C., Freeland, H. J., Roemmich, D., Wijffels, S., Troisi, A., Belbéoch, M., ... & Jayne, S.  
718 R. (2016). Fifteen years of ocean observations with the global Argo array. *Nature Climate*  
719 *Change*, 6(2), 145-153
- 720 Simon, J. D., Simons, F. J., & Irving, J. C. (2021). A MERMAID miscellany: Seismoacoustic  
721 signals beyond the P wave. *Seismological Society of America*, 92(6), 3657-3667.
- 722 Smith, D. K., Tolstoy, M., Fox, C. G., Bohnenstiehl, D. R., Matsumoto, H., & J. Fowler, M. (2002).  
723 Hydroacoustic monitoring of seismicity at the slow-spreading Mid-Atlantic Ridge. *Geophysical*  
724 *Research Letters*, 29(11), 13-1.
- 725 Sladen, A., Rivet, D., Ampuero, J. P., De Barros, L., Hello, Y., Calbris, G., & Lamare, P. (2019).  
726 Distributed sensing of earthquakes and ocean-solid Earth interactions on seafloor telecom  
727 cables. *Nature communications*, 10(1), 1-8
- 728 Spica, Z. J., Nishida, K., Akuhara, T., Pétrélis, F., Shinohara, M., & Yamada, T. (2020). Marine  
729 sediment characterized by ocean-bottom fiber-optic seismology. *Geophysical Research*  
730 *Letters*, 47(16), e2020GL088360.
- 731 Talandier, J., & Okal, E. A. (2001). Identification criteria for sources of T waves recorded in  
732 French Polynesia. In *Monitoring the Comprehensive Nuclear-Test-Ban Treaty:*  
733 *Hydroacoustics* (pp. 567-603). Birkhäuser, Basel.
- 734 Talandier, J., Hyvernaud, O., Reymond, D., & Okal, E. A. (2006). Hydroacoustic signals generated  
735 by parked and drifting icebergs in the Southern Indian and Pacific Oceans. *Geophysical Journal*  
736 *International*, 165(3), 817-834.
- 737 Talandier, J., & Okal, E. A. (2016). A new source discriminant based on frequency dispersion for  
738 hydroacoustic phases recorded by T-phase stations. *Geophysical Journal International*, 206(3),  
739 1784-1794.
- 740 Tepp, G., & Dziak, R. P. (2021). The seismo-acoustics of submarine volcanic eruptions. *Journal*  
741 *of Geophysical Research: Solid Earth*, 126(4), e2020JB020912.
- 742 Tolstoy, I., & Ewing, M. (1950). The T phase of shallow-focus earthquakes. *Bulletin of the*  
743 *Seismological Society of America*, 40(1), 25-51.
- 744 Tréhu, A. M., Wilcock, W. S., Hilmo, R., Bodin, P., Connolly, J., Roland, E. C., & Braunmiller,  
745 J. (2018). The role of the Ocean Observatories Initiative in monitoring the offshore earthquake  
746 activity of the Cascadia subduction zone. *Oceanography*, 31(1), 104-113.
- 747 Uchida, N., & Bürgmann, R. (2019). Repeating earthquakes. *Annual Review of Earth and*  
748 *Planetary Sciences*, 47(1), 305-332.
- 749 Ugalde, A., Becerril, C., Villaseñor, A., Ranero, C. R., Fernández-Ruiz, M. R., Martín-Lopez, S., ...  
750 & Martins, H. F. (2022). Noise Levels and Signals Observed on Submarine Fibers in the Canary  
751 Islands Using DAS. *Seismological Society of America*, 93(1), 351-363

- 752 Viens, L., Bonilla, L. F., Spica, Z. J., Nishida, K., Yamada, T., & Shinohara, M. (2022). Nonlinear  
753 earthquake response of marine sediments with distributed acoustic sensing. *Geophysical Research*  
754 *Letters*, *49*(21), e2022GL100122.
- 755 Walker, D. A., McCreery, C. S., & Hiyoshi, Y. (1992). T-phase spectra, seismic moments, and  
756 tsunamigenesis. *Bulletin of the Seismological Society of America*, *82*(3), 1275-1305.
- 757 Webb, S. C. (1998). Broadband seismology and noise under the ocean. *Reviews of*  
758 *Geophysics*, *36*(1), 105-142.
- 759 Withers, M., Aster, R., Young, C., Beiriger, J., Harris, M., Moore, S., & Trujillo, J. (1998). A  
760 comparison of select trigger algorithms for automated global seismic phase and event  
761 detection. *Bulletin of the Seismological Society of America*, *88*(1), 95-106.
- 762 Wilcock, W. S., Abadi, S., & Lipovsky, B. P. (2023). Distributed acoustic sensing recordings of  
763 low-frequency whale calls and ship noise offshore Central Oregon. *JASA Express Letters*, *3*(2),  
764 026002.
- 765 Williams, E. F., Fernández-Ruiz, M. R., Magalhaes, R., Vanthillo, R., Zhan, Z., González-Herráez,  
766 M., & Martins, H. F. (2019). Distributed sensing of microseisms and teleseisms with submarine  
767 dark fibers. *Nature communications*, *10*(1), 1-11.
- 768 Williams, E. F., Fernández-Ruiz, M. R., Magalhaes, R., Vanthillo, R., Zhan, Z., González-Herráez,  
769 M., & Martins, H. F. (2021). Scholte wave inversion and passive source imaging with ocean-  
770 bottom DAS. *The Leading Edge*, *40*(8), 576-583.
- 771 Williams, E. F., Zhan, Z., Martins, H. F., Fernandez-Ruiz, M. R., Martin-Lopez, S., Gonzalez-  
772 Herraez, M., & Callies, J. (2022). Surface gravity wave interferometry and ocean current  
773 monitoring with ocean-bottom DAS. *Journal of Geophysical Research: Oceans*, e2021JC018375
- 774 Wunsch, C. (2016). Global ocean integrals and means, with trend implications. *Annual Review of*  
775 *Marine Science*, *8*, 1-33.
- 776 Wech, A., Tepp, G., Lyons, J., & Haney, M. (2018). Using earthquakes, T waves, and infrasound  
777 to investigate the eruption of Bogoslof volcano, Alaska. *Geophysical Research Letters*, *45*(14),  
778 6918-6925.
- 779 Wu, W., Zhan, Z., Peng, S., Ni, S., & Callies, J. (2020). Seismic ocean  
780 thermometry. *Science*, *369*(6510), 1510-1515.
- 781 Yu, C., Day, E. A., de Hoop, M. V., Campillo, M., & van der Hilst, R. D. (2017). Mapping mantle  
782 transition zone discontinuities beneath the Central Pacific with array processing of SS  
783 precursors. *Journal of Geophysical Research: Solid Earth*, *122*(12), 10-364.
- 784 Zhan, Z. (2020). Distributed acoustic sensing turns fiber-optic cables into sensitive seismic  
785 antennas. *Seismological Research Letters*, *91*(1), 1-15.
- 786 Zhang, J., & Langston, C. A. (2020). Separating the scattered wavefield from teleseismic P using  
787 curvelets on the long beach array data set. *Geophysical Journal International*, *220*(2), 1112-1127.
- 788 Zhou, Y., Chen, X., Ni, S., Qian, Y., Zhang, Y., Yu, C., ... & Xu, M. (2021). Determining crustal  
789 attenuation with seismic T waves in southern Africa. *Geophysical Research Letters*, *48*(15),  
790 e2021GL094410